Chemical Engineering Journal 425 (2021) 130603

Contents lists available at ScienceDirect

Chemical Engineering Journal

journal homepage: www.elsevier.com/locate/cej

Dimensional engineering of carbon dots derived sulfur and nitrogen co-doped carbon as efficient oxygen reduction reaction electrocatalysts for aluminum-air batteries

Ruiqi Cheng, Min Jiang, Kaiqi Li, Meilin Guo, Jiao Zhang *, Jianming Ren, Pengyu Meng, Runhua Li, Chaopeng Fu *

School of Materials Science and Engineering, Shanghai Jiao Tong University, Shanghai 200240, PR China

ARTICLE INFO

Keywords:
Al-air battery
Oxygen reduction reaction
Carbon dots
Dimensional engineering

ABSTRACT

The sluggish kinetics of oxygen reduction reaction (ORR) on the cathode limits the development of metal-air batteries and fuel cells. In this work, N, S doped carbon materials with one dimensional (1D) microrod, two dimensional (2D) nanosheet and three dimensional (3D) framework structures prepared using nitrogen-doped carbon dots as precursors are studied as electrocatalysts to improve the ORR performance. The carbon dots with the unique properties are crucial in forming the designed structure, and the formation mechanism of the dimensional carbon materials is revealed. The ORR performance is investigated in both alkaline and neutral electrolytes, and the results reveal that the two-dimensional N, S doped carbon nanosheets (2D N-S-CNS) show better ORR performance than the 1D or 3D counterparts, which is mainly attributed to the higher heteroatoms doping amount. In addition, the ORR performance of 2D N-S-CNS is comparable to that of Pt/C. To reveal the practical application, the carbon electrocatalysts are also studied in aluminum-air (Al-air) batteries, and the Al-air batteries based on 2D N-S-CNS display larger power density and higher working voltage than those with Pt/C in both KOH and NaCl electrolytes.

1. Introduction

Oxygen reduction is a key reaction in fuel cells and metal-air batteries, however, the intrinsic sluggish kinetics significantly limits the performance of these air-breathing energy conversion systems [1]. Therefore, efficient electrocatalysts are required to reduce the reaction energy barrier and boost the reaction rate of oxygen reduction reaction (ORR). Currently, Pt/C catalyst is well-known as the most efficient electrocatalyst for ORR [2,3]. However, the limited nature reserve and high cost of Pt significantly restrain its large-scale application [1]. To solve this problem, non-precious-metal electrocatalysts (like carbon-based materials, metal oxides, spinel, perovskite etc.) are developed as low-cost substitutes for Pt-based electrocatalysts [4]. Among them, carbon materials with good stability, high electrical conductivity, large surface areas and facile manipulation have received great interest for ORR [5,6].

Intrinsic carbon materials exhibit relative low ORR catalytic activity, and heterogeneous doping of carbon is known as an effective strategy to boost ORR catalytic activity by polarizing the adjacent carbon atoms due to the different electronegativity [7,8]. Several heteroatoms like B, N, P, S and F in carbon matrix have been proved for improving ORR activity, as the doped carbon can facilitate the adsorption of oxygen species to promote ORR [9–13]. N is the most widely used heteroatom for carbon doping, and a series of nitrogen-doped carbon electrocatalysts present excellent ORR performance [14]. A 3D N-doped carbon network with a high N doping content of 8.14% derived from metal organic frameworks demonstrated a highly catalytic activity close to Pt/C [15]. Hierarchically porous carbon plates constructed from enzyme displayed enhanced ORR performance [16]. Although a series of strategies for synthesizing N-doped carbon electrocatalysts have been raised, the activities of most N-doped carbon catalysts are unsatisfied due to the limited active sites. Hence, it is suggested other heteroatoms are needed to further enhance the ORR catalytic activity [17]. S with slightly higher electronegativity than carbon is also wildly used for carbon doping, as the S doping can modify the electron distribution of the carbon matrix to create active sites [18,19]. It is expected that the co-doping of S and N in

* Corresponding authors at: School of Materials Science and Engineering, Shanghai Jiao Tong University, Shanghai 200240, PR China.
E-mail addresses: zj119@sjtu.edu.cn (J. Zhang), chaopengfu@sjtu.edu.cn (C. Fu).

https://doi.org/10.1016/j.cej.2021.130603
Received 8 March 2021; Received in revised form 12 May 2021; Accepted 27 May 2021
Available online 2 June 2021

carbon can contribute to excellent ORR catalytic activity.

In addition, the ORR activities of electrocatalysts also rely on their structures and morphologies [20], and tuning the dimension of carbon materials provides the possibility of manipulating the electrocatalytic performance. Carbon materials with different dimensions can be prepared through choosing appropriate raw materials [10,21,22]. Carbon dots (CDs) with unique structure are identified as tunable precursors for preparing carbon materials. However, due to the large surface energy, carbon dots tend to aggregate into carbon bulk with a low specific surface area, resulting in an unsatisfied catalytic activity [23,24]. So far, limited studies focus on the synthesis of carbon dots derived carbon used as electrocatalysts. Moreover, the ORR catalytic activity of the carbon electrocatalyst derived from carbon dots are far from the Pt/C [25,26], which is mostly due to the low specific surface area and limited active sites. Therefore, new strategies are required to modify the structure of the carbon derived from carbon dots. Templated synthesis using a pre-existing guide with desired structure features is capable of preparing materials with unique structures, morphologies and properties. It is therefore considered that the combination of carbon dots and template may provide great opportunities for preparing unique carbon electrocatalysts with superior ORR performance.

Herein, we prepare a series of carbon dots derived carbon materials with N, S doping and different dimensions through a template-assisted strategy. Carbon materials with one dimensional (1D) microrod, two dimensional (2D) nanosheet and three dimensional (3D) framework structures have been prepared using nitrogen-doped carbon dots as precursors. The carbon dots with the unique properties are crucial in forming the designed structure, and the formation mechanism of the dimensional carbon materials is revealed. The various dimensional carbon materials are studied as electrocatalysts for oxygen reduction reaction (ORR) in both alkaline and neutral electrolytes, and the results reveal that the 2D N, S doped carbon nanosheets (2D N-S-CNS) show better ORR performance than their 1D or 3D counterparts, and the ORR performance of 2D N-S-CNS is comparable to that of Pt/C. Furthermore, the carbon electrocatalysts are also studied in Al-air batteries to reveal the practical application, and the Al-air batteries based on 2D N-S-CNS display larger power density and higher working voltage than that with Pt/C in both KOH and NaCl electrolytes.

2. Experimental sections

2.1. Synthesis of nitrogen and sulfur doped carbon with different dimensions

Typically, 5 g of citric acid was dissolved in 50 mL of deionized water, then 5 mL of $NH_3{\cdot}H_2O$ was dropped into the solution and stirred for 30 mins. Subsequently, the solution was transferred into an autoclave (100 mL) and treated at 180 °C for 12 hrs. Then the solution was centrifuged to remove large particles and dialyzed for 2 days, the obtained solution was dried in an oven at 120 °C for 24 hrs to achieve the nitrogen doped carbon dots (NCDs) powder. 0.15 g of NCDs, 0.03 g of thiourea and 0.3 g of template (Fe_2O_3 or NaCl or SiO_2) were dispersed in 10 mL of deionized water and stirred for 1 h, and the mixture was frozen with liquid nitrogen following freezing drying for 24 hrs. Then, the sample was heated at 300 °C for 1 h with a ramp of 5 °C min^{-1} and further pyrolyzed at 900 °C for 4 hrs with a ramp rate of 10 °C min^{-1} under N_2 atmosphere. The resultant product was washed with 2 M HCl, deionized water or 20% HF to remove the template. The products obtained by using Fe_2O_3, NaCl and SiO_2 were denoted as one-dimensional N,S co-doped carbon microrods (1D N-S-CMR), two-dimensional N,S co-doped carbon nanosheets (2D N-S-CNS) and three-dimensional N,S co-doped carbon frameworks (3D N-S-CFW), respectively. Also, the N,S co-doped carbon (denoted as N-S-C) was synthesized with the identical procedure but without adding any template.

2.2. Materials characterizations

Fourier transform infrared (FTIR) was measured on Fourier transform infrared spectrometer (IR Nicolet 6700) and Uv/vis was measured on UV–VIS-NIR Spectrophotometer (Lamda 950). Scanning electron microscopy (SEM) images were obtained with Mira 3 scanning electron microscope. Transmission electron microscope (TEM), high-angle annular dark-field scanning transmission electron microscope (HADDF-STEM) images and elemental mappings were obtained with TALOS F200X Field emission transmission electron microscope. Raman spectra were sketched by testing data acquired using confocal microprobe Raman spectroscopy (inVia Qontor). Brunauer-Emmett-Teller (BET) measurement was tested by fully automatic specific surface and porosity analyzer (ASAP 2020 HD 88). X-ray photoelectron spectroscopy (XPS) was conducted on Axis Ultra DLD Kratos AXIS SUPRA. Thermo gravimetric analysis (TGA) and differential scanning calorimetry (DSC) were conducted on thermo gravimetric analyzer (TGA Pyris 1).

2.3. Electrochemical measurements

Cyclic voltammetry (CV) and linear sweep voltammetry (LSV) measurements were performed at a sweep speed of 10 mV s^{-1} with a three-electrode configuration using potentiostatic (Gamry Ref 600 +). Rotating disk electrode (RDE, $d = 5$ mm) covered with electrocatalyst served as working electrode, whereas the saturated calomel electrode (SCE) and graphite rod were served as reference and counter electrodes, respectively. The catalyst ink was prepared by mixing 2 mg of catalyst in 240 μL ethanol, 240 μL deionized water and 20 μL Nafion (5%) and sonicating for 30 min, followed by dropping 20 μL of suspension onto the polished glassy carbon electrode and dry under the infrared light. The electrolyte is either O_2-saturated KOH solution (0.1 M) or NaCl solution (3.5 wt%). All potentials in this work were transformed against the reversible hydrogen electrode (RHE).

$$E_{RHE} = E_{SCE} + E^0_{SCE} + 0.059{*}pH \quad (E^0_{SCE} = 0.2413V)$$

In 0.1 M KOH solution, $E_{RHE} = E_{SCE} + 1.0083$ V
In 3.5% NaCl solution, $E_{RHE} = E_{SCE} + 0.6543$ V

2.4. Al-air battery testing

The air cathode was prepared by mixing the active electrocatalyst (2D N-S-CNS), carbon Vulcan XC-72 and poly-tetrafluoroethylene (PTFE, 60 wt% emulsion) with a mass ratio of 20: 60: 20 in ethanol, and the mixture was stirred to form to a film, which was then pressed onto Ni foam current collector. The gas diffusion layer was prepared with the composition of PTFE and carbon Vulcan xc-72 and pressed onto the other side of the Ni foam current collector. The three-layer electrode was then pressed under 40 MPa pressure for 5 min to achieve the air cathode with a catalyst mass loading of approximately 2.1 mg cm^{-2}. The anode was the polished Al-1.0 wt% Mg-0.1 wt% Sn plate, which was casted using high purity aluminum (99.99 wt%), magnesium particles and tin particles (99.99%) at a temperature of 760 ± 5 °C in a resistance furnace. The electrolyte was either 4 M NaOH solution or 3.5% NaCl. The discharge testing of the Al-air batteries was conducted on LAND testing system (LAND Electronics Ltd.).

3. Results and discussion

Firstly, the NCDs were prepared, and the synthetic route is illustrated in Fig. S1a. Citric acid was used as the precursor to prepare the carbon dots via a bottom-up synthesis, while ammonia ($NH_3{\cdot}H_2O$) was served as the N doping source. The yield of the NCDs is 1.2 wt%. The NCDs with an average size of approximately 4 nm present uniform atomic arrangement (Fig. S1b), and the clearly observed lattice fringes are attributed to the high degree of crystallinity of NCDs (Fig. S1c) [27,28]. The blurred

boundary of the NCDs may be caused by the introduction of functional groups on amorphous carbon areas [29]. Fig. S1d shows the photoluminescence (PL) curves, and the fluorescent yield was determined to be 11.4%. Moreover, the NCDs show excitation–dependent multi-color emissive behavior. Furthermore, the XRD pattern of the NCDs displaying two peaks at 24.2° and 43.2° are ascribed to (0 0 2) and (1 0 1) planes in Fig. S1e, respectively, suggesting the moderate graphitic structure of the synthesized NCDs [30]. The results clearly demonstrate the successful synthesis of the NCDs with unique features. Then, Fe_2O_3 microrods, NaCl and SiO_2 spheres were chosen as the templates to prepare the various dimensional carbon materials. Fe_2O_3 rods were used as the one-dimensional template, and the final product N,S co-doped carbon microrods (denoted as N-S-CMR) clearly shows the one-dimensional microrod structure in Fig. 1a, b. Then, NaCl was used as the template to prepare two-dimensional carbon, the formed N,S co-doped carbon (denoted as N-S-CNS) shows a two-dimensional thin-layer nanosheet structure (Fig. 1 c, d). SiO_2 spheres were used as templates to prepared the three-dimensional carbon, as the SiO_2 spheres were stacked together to form a three dimensional structure. The resultant N,S co-doped carbon (denoted as N-S-CFW) shows a three-dimensional honey-comb like network structure (Fig. 3e, f). All the formed carbon products well inherit the template structure, and the formation mechanisms of the 1D N,S co-doped carbon microrods, 2D N,S co-doped carbon nanosheets and 3D N,S co-doped carbon framework are illustrated in Fig. 1g. The formation of the 1D, 2D and 3D carbon materials can be divided into three steps. Firstly, the carbon dots were congregated and covered on the surface of the templates. Then, the congregated NCDs clusters covered on the template surfaces were converted to the corresponding carbon materials during the pyrolysis at a high temperature. Finally, the templates were removed to obtain the corresponding carbon materials with the inherited morphologies.

Both the NCDs and templates play important roles in forming the designed morphologies of the carbon materials. When the NCDs were directly pyrolyzed without any template, the formed N,S doped carbon (denoted as N-S-C) displays irregular bulk structure (Fig. S2), indicating the role of the template in directing the formation of the dimensional carbon material. More importantly, the carbon dots are also critical for forming the carbon materials with various dimensions. In order to probe

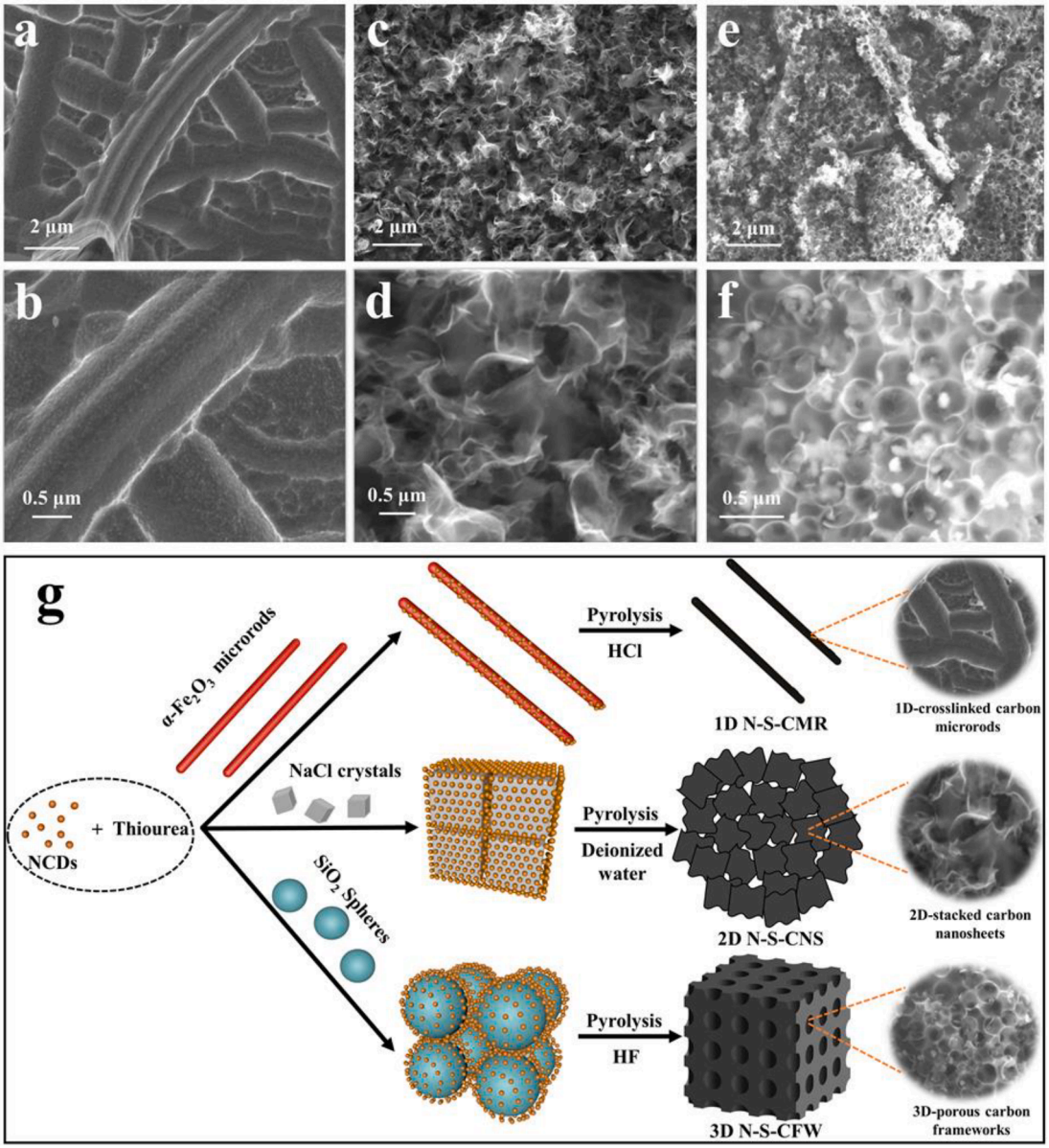

Fig. 1. Low and high magnification SEM images of (a, b) 1D N-S-CMR, (c, d) 2D N-S- CNS, and (e, f) 3D N-S-CFW. (g) schematic synthesis of 1D N-S-CMR, 2D N-S-CNS, and 3D N-S-CFW.

the role of carbon dots, citric acid (CA), the precursor of carbon dots, was used to prepare the carbon materials with the same template (Fe_2O_3 rods, NaCl or SiO_2 spheres), and the obtained N,S doped carbon materials are denoted as NSC-1, NSC-2 and NSC-3, respectively (The preparations are shown in the Supplementary data). The NSC-1 is composed of inhomogeneous carbon particles (Fig. S3a, b), which is different from the morphology of the template. The NSC-2 exhibits a 2D sheet-like structure but with a larger thickness (Fig. S3c,d). The NSC-3 shows star-like structure (Fig. S3e,f). Obviously, the morphologies of the carbon materials derived from CA are significantly different from those derived from the carbon dots, and they didn't inherite the morphologies of their templates. It is deduced that the formation mechanism is different here, and Fig. S3g illustrates the possible synthesis and forming mechanism. It can be explained that the congregation degree of NCDs is high due to the high surface energy and low content of functional groups, and the NCDs can mostly cover the surface of the template, while the CA cannot fully cover the surface of the template due to the low congregation degree. The SiO_2 sphere template is then taken as an example to support this. The SEM image of the precursors for 3D N-S-CFW (the mixture of NCDs, thiourea and SiO_2) shows that the SiO_2 spheres are mostly covered by the NCDs (Fig. S4a, b), while the SEM image of the precursors for NSC-3 (the mixture of CA, thiourea and SiO_2) shows that only a portion of SiO_2 spheres are covered by the CA (Fig. S4c, d). The corresponding elemental mappings also confirm this, and the carbon element is uniformly distributed (Fig. S5). When the template is partially covered with CA, the derived NSC-1, NSC-2 and

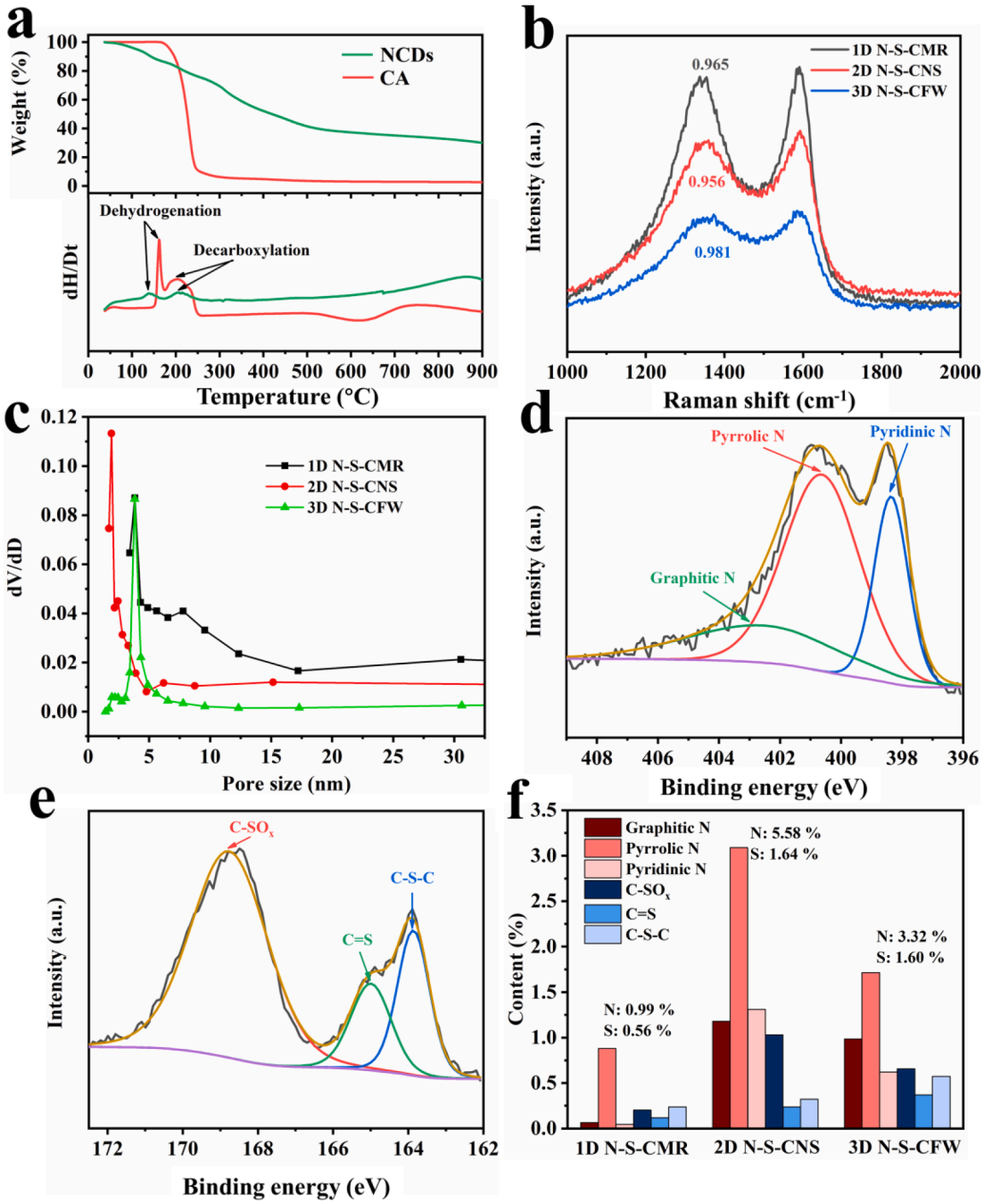

Fig. 2. (a) TGA/DSC curves of NCDs and CA, (b) Raman spectra and (c) pore size distribution of 1D N-S-CMR, 2D N-S-CNS and 3D N-S-CFW, (d) N1s and (e) S2p XPS of 2D N-S-CNS, (f) the fractions of different N and S species in each sample.

NSC-3 show particle, thick and inhomogeneous, and star-like morphologies, respectively. When the template is fully covered with the NCDs, the derived carbon materials inherit the morphologies and display 1D, 2D, and 3D structures.

The TGA and DSC curves of the NCDs and CA are shown in Fig. 2a. The mass loss of CA is nearly 90% within the temperature range of 150–300 °C, and the peaks at ~160 °C and ~200 °C are ascribed to dehydrogenation and decarboxylation, respectively [31]. The result confirms that there is a high content of oxygen-containing functional groups like –OH and –COOH in CA. On the contrary, the mass loss of NCDs decreases gradually throughout the temperature region of 100–500 °C, and no obvious peaks are observed. The result suggests the NCDs contain less functional groups, and the remained carbon after pyrolysis is much higher in the NCDs than CA. Additionally, the various oxygen-containing functional groups in NCDs are confirmed by FTIR in Fig. S6, and the π–π^* transition of graphitic sp^2 domains in the NCDs is confirmed by the peak at 330 nm in Uv/vis curve (Fig. S7) [32]. The O and N contents of the NCDs measured by XPS are 24.0% and 7.7%, respectively (Fig. S8). Therefore, the total content of N and O in the NCDs is much lower than the O content in CA (58.3%). The lower content of functional groups may explain the higher congregation degree of the NCDs compared with CA.

The Raman spectra of 1D N-S-CMR, 2D N-S-CNS and 3D N-S-CFW in Fig. 2b show two obvious bands at 1350 cm^{-1} corresponding to the D band and at 1580 cm^{-1} corresponding to the G band for sp^2-hybridized carbon [33]. Meanwhile, the 2D N-S-CNS shows the smallest value of I_D/I_G, indicating that the highest graphitization degree [34]. The nitrogen adsorption isotherms of the different carbon materials are shown in Fig. S9, and all the samples display a type-IV isotherm with a H3-type hysteresis loop, indicating mesoporous structure [35]. The BET surface areas of 1D N-S-CMR, 2D N-S-CNS and 3D N-S-CFW are 793.5, 521.4, 164.4 $m^2\ g^{-1}$, respectively, and the pore volumes of 1D N-S-CMR, 2D N-S CNS and 3D N-S CFW are 0.955, 1.359, and 3.228 cc g^{-1}, respectively. The pore distribution curves are shown in Fig. 2c. The 1D N-S-CMR containing mesopores with diameters of 4.0 nm and 7.8 nm displays the largest specific surface area. The 2D N-S-CNS containing mesopores with diameters of 2.0 nm and 6.1 nm displays a relatively smaller specific surface area. The 3D N-S-CFW containing mesopores with diameters of 2.2 nm and 4.0 nm displays the smallest specific surface area.

The XRD pattern of 2D N-S-CNS in Fig. S10 shows two obvious peaks at ~24° and ~43°, corresponding to (002) and (101) planes of graphitic carbon [36]. The XPS survey scan of in Fig. S11 confirms the elements of carbon, nitrogen, oxygen and sulfur in the 2D N-S-CNS shown, indicating the successful doping of nitrogen and sulfur in the carbon. The deconvoluted N1s spectrum in Fig. 2d shows three peaks at ~ 398.4, 400.6 and 402.5 eV, corresponding to pyridinic N, pyrrolic N and graphitic N, respectively [37]. The deconvoluted S 2p spectrum in Fig. 2e also shows three peaks at 163.8, 165.0 and 168.6 eV, corresponding to C-S-C, C = S and C-SO_x, respectively [38]. The deconvoluted N 1 s and S 2p spectra of 1D N-S-CMR and 3D N-S-CFW are shown in Fig. S12, and the contents of all the N and S species are summarized in Fig. 2f. The 2D N-S-CNS possesses the highest content of N and S (N:5.58% and S: 1.64%), while the 1D N-S-CMR possesses the lowest content of N and S (N:0.99% and S: 0.56%). The different doping amounts in the carbon materials are ascribed to the different templates. The molten NaCl could seal the precursors very well, and loss of N and S was suppressed during the pyrolysis. Therefore, the 2D N-S-CNS displays the highest doping content. The SiO_2 template could not seal the precursors, and part of N and S species was evaporated during the pyrolysis, resulting in the moderate doping content in the 3D N-S-CFW. The Fe_2O_3 template was partially reduced to FeO and FeS by thiourea during the pyrolysis, which is confirmed by XRD (Fig. S13). As partial thiourea was consumed by the reduction, the 1D N-S-CMR displays the lowest doping content. The higher doping amount can create more active sites for the ORR. Moreover, the 2D N-S-CNS displays the highest contents of pyridinic N and pyrrolic N, which are the most active sites for ORR [39]. Additionally, the 2D N-S-CNS displays the highest content of -SO_x- specie, which is at the edges of the carbon matrix and can be fully exposed [40]. Furthermore, this oxygen-containing functional group (-SO_x- specie) can improve the wettability of the carbon to facilitate oxygen adsorption [41].

The morphologies of 1D N-S-CMR, 2D N-S-CNS, and 3D N-S-CFW are further displayed in the TEM images. Fig. 3a clearly shows the 2D thin-layer nanosheet structure of the N-S-CNS, and the graphene-like thin layer of the carbon nanosheet is observed in Fig. 3b. The average thickness of nanosheets is determined to be ~6.0 nm (Fig. S14). Additionally, the TEM images of 1D N-S-CMR and 3D N-S-CFW are shown in Fig. S15. The N-S-CMR displays the 1D microrod structure with a width of ~100 nm (Fig. S15a). The N-S-CFW displays the spheres-stacked 3D structure, and the diameter of the sphere is ~200 nm (Fig. S15b). Fig. 3c-f shows the HADDF-STEM with element mappings of 2D N-S-CNS, and the C, N and S elements are homogeneously distributed in the carbon nanosheets, further confirming the successful doping of N and S in the carbon matrix.

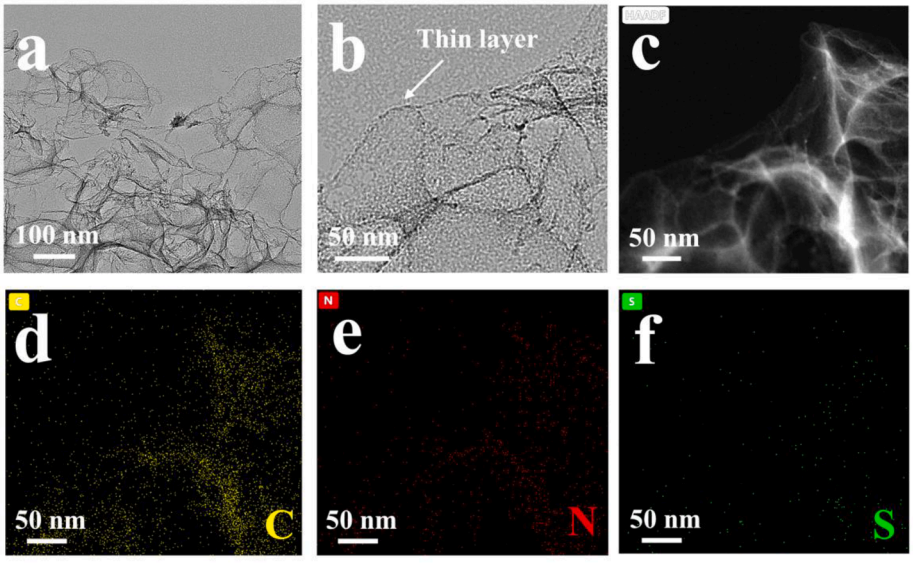

Fig. 3. (a, b) TEM images with low and high magnifications and (c) HAADF-STEM image of 2D N-S-CNS, (d, e, f) the corresponding element mappings.

The oxygen reduction activities of the 1D N-S-CMR, 2D N-S-CNS, 3D N-S-CFW and N-S-C were evaluated in 0.1 M KOH. The CV curves of the 1D N-S-CMR, 2D N-S-CNS and 3D N-S-CFW in Fig. 4a display clear reduction peaks, indicating the oxygen reduction. Meanwhile, there is no obvious reduction peak of the N-S-C, indicating a low ORR catalytic activity. The reduction peak potentials on 1D N-S-CMR, 2D N-S-CNS and 3D N-S-CFW are 0.753 V, 0.841 V and 0.761 V, respectively, and the most positive peak potential suggests the most efficient oxygen reduction of the 2D N-S-CNS. The LSV curves of the different samples are shown in Fig. 4b, and the extracted onset potentials (E_{onset}) and half wave potentials ($E_{1/2}$) are listed in Table S1. The 2D N-S-CNS exhibits the most positive onset potential (E_{onset} = 0.957 V) and $E_{1/2}$ (0.855 V), which are comparable to those of the commercial Pt/C (E_{onset} is 0.985 V and $E_{1/2}$ is 0.852 V). Moreover, the LSV curves of the different reference groups derived from CA are also exhibited and compared with those of 1D N-S-CMR, 2D N-S-CNS and 3D N-S-CFW (Fig. S16), the 1D N-S-CMR and 2D N-S-CNS exhibit better ORR performance than their counterparts. Fig. 4c is the fitted Tafel slopes of different samples in alkaline solutions, and the 2D N-S-CNS possesses the lowest Tafel slope (94.5 mV dec^{-1}), indicating the fast kinetics. Fig. 4d shows the electrochemical surface area (ECSA), electron transfer number (n) and kinetic current density (J_k) of 1D N-S-CMR, 2D N-S-CNS and 3D N-S-CFW, the details of the calculation are provided in the Supplementary data (Fig. S17). The largest ESCA of 2D N-S-CNS demonstrates the most exposed active sites, which promotes the kinetics of ORR [42]. Moreover, the largest J_k indicates the greatest intrinsic activity of the 2D N-S-CNS catalyst [43]. The electron transfer number of 2D N-S-CNS is 3.98, suggesting a four-electron pathway of the ORR on 2D N-S-CNS. Fig. 4e shows that the

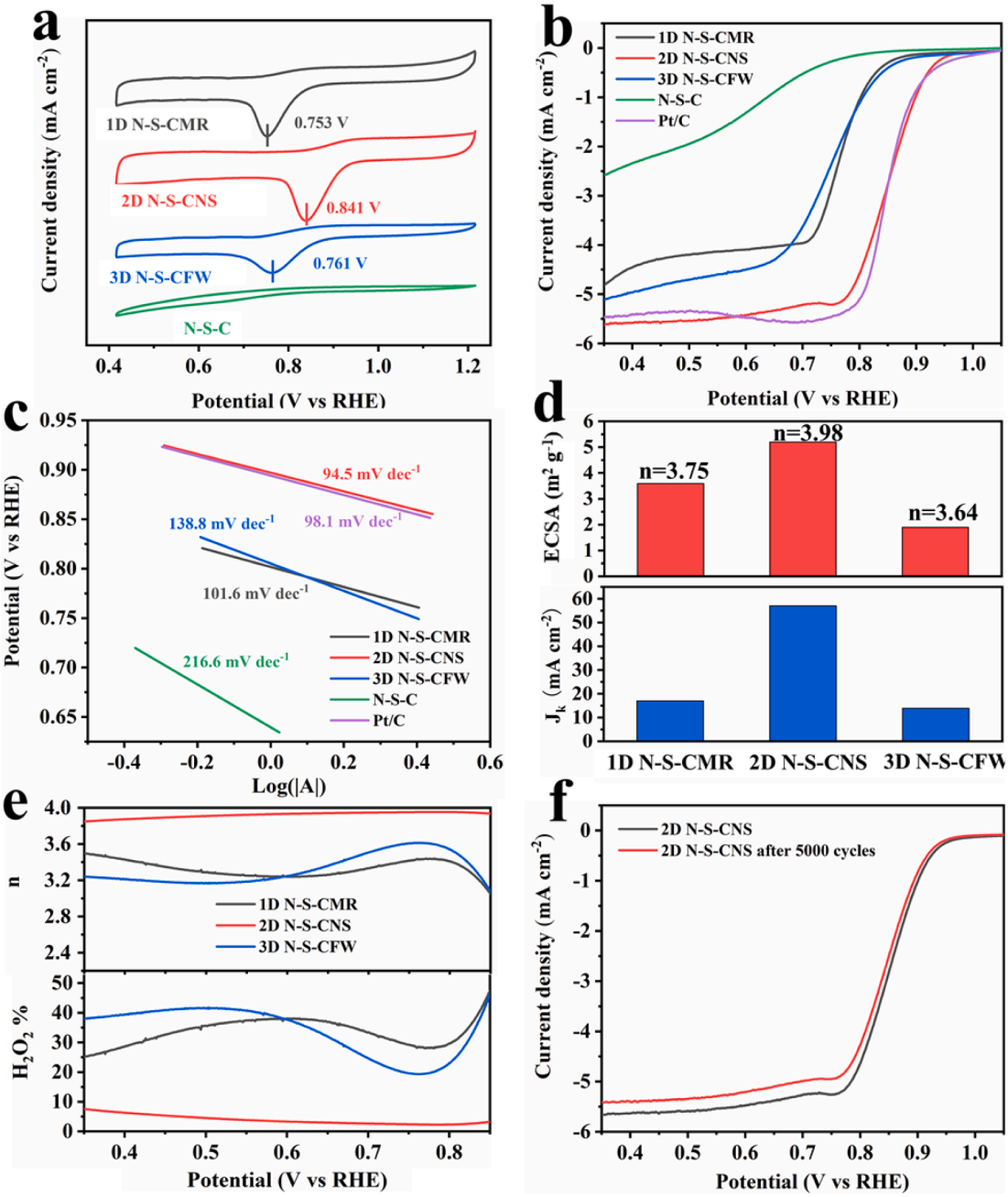

Fig. 4. (a) CV curves, (b) LSV curves, and (c) the corresponding Tafel plots of the 1D N-S-CMR, 2D N-S-CNS and 3D N-S-CFW in 0.1 M KOH alkaline solution. (d) ECSA and J_k, (e) H_2O_2 yields and electron transfer number of 1D N-S-CMR, 2D N-S-CNS and 3D N-S-CFW. (f) LSV curves before and after 5000 cycles of 2D N-S-CNS in a 0.1 M KOH solution.

H_2O_2 yield on 2D N-S-CNS is the lowest (below 10%), further confirming that the main reaction during ORR undergoes the four-electron pathway [44]. Fig. 4f shows that the LSV curves of 2D N-S-CNS before and after 5000 cycles are nearly the same, suggesting the superior durability of the electrocatalyst. Table S2 shows the ORR performance comparison of the N-S-CNS with others in recent literature, and the onset and have-wave potentials of the N-S-CNS is competitive to most of the others. The best performance of the 2D N-S-CNS is explained that it possesses the highest heteroatom content and largest ECSA, suggesting the mostly highly available active sites for ORR.

The oxygen reduction performance of these dimensional carbon electrocatalysts was also evaluated in a 3.5% NaCl neutral solution. The CV curves of 1D N-S-CMR, 2D N-S-CNS, 3D N-S-CFW and N-S-C are presented in Fig. 5a, and the reduction peak potential of 2D N-S-CNS (0.594 V) is the most positive, indicating a prominent ORR performance. The LSV curves of the various samples as well as commercial Pt/C are shown in Fig. 5b, and the extracted onset potentials (E_{onset}) and half-wave potentials ($E_{1/2}$) are listed in Table S3. The onset and half-wave potentials of 2D N-S-CNS are 0.742 V and 0.604 V, respectively, which are more positive than those of Pt/C (0.684 V and 0.564 V). Meanwhile, the LSV curves of 1D N-S-CMR, 2D N-S-CNS and 3D N-S-CFW electrocatalysts are also shown and compared with these of their counterparts derived from CA in Fig. S18. Similar to the results in the alkaline solution, the 1D N-S-CMR and 2D N-S-CNS exhibit better ORR performance

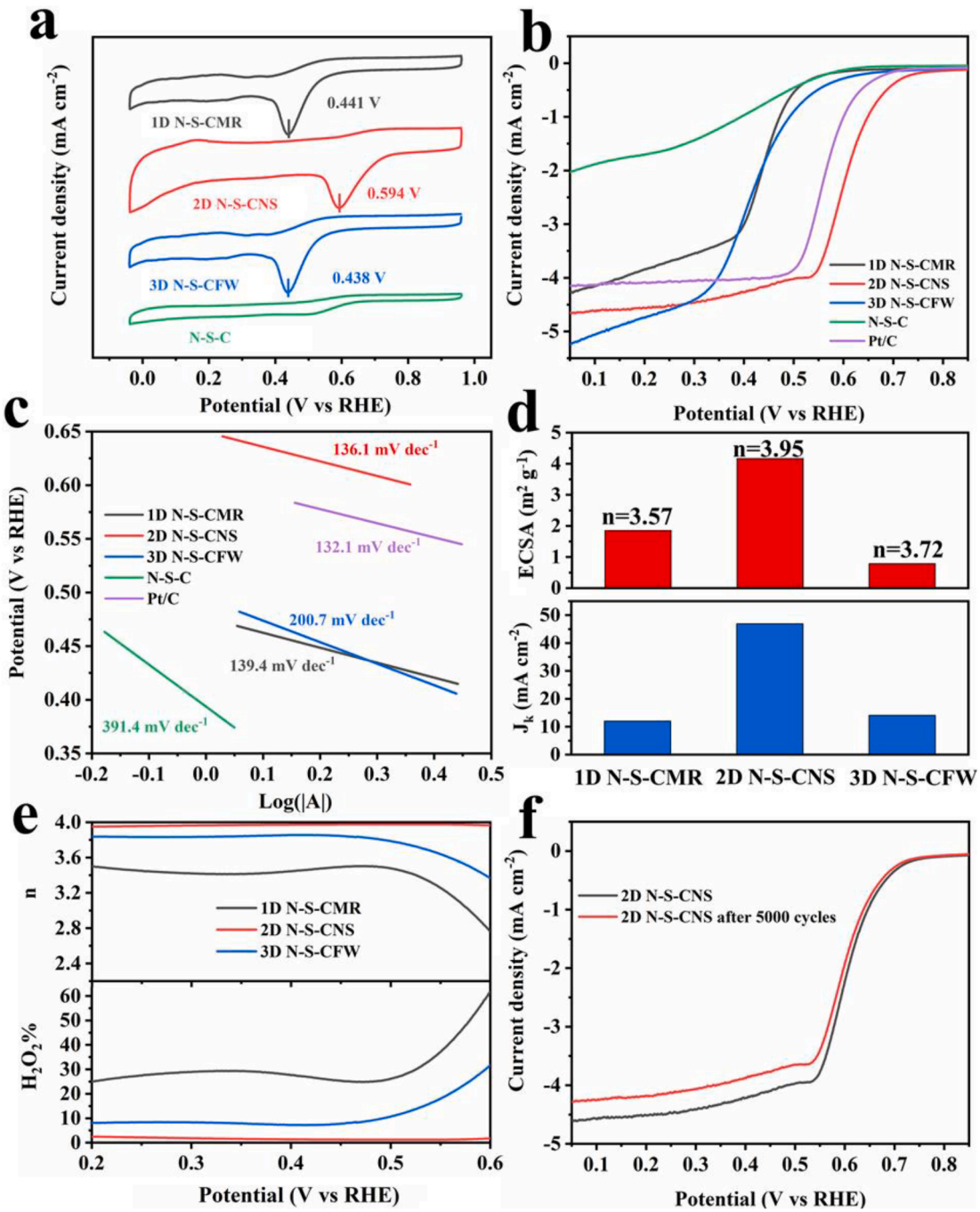

Fig. 5. (a) CV curves, (b) LSV curves, and (c) the corresponding Tafel plots of the 1D N-S-CMR, 2D N-S-CNS and 3D N-S-CFW in 3.5% NaCl neutral solution. (d) ECSA and J_k, (e) H_2O_2 yields and electron transfer number of 1D N-S-CMR, 2D N-S-CNS and 3D N-S-CFW. (f) LSV curves before and after 5000 cycles of 2D N-S-CNS in a 3.5% NaCl solution.

than their counterparts, and the NSC-3 shows a more positive half-wave potential than 3D N-S-CFW. Fig. 5c shows the Tafel slopes of the different samples, and the 2D N-S-CNS possesses the Tafel slope of 136.1 mV dec^{-1}, which is the close to that of Pt/C (132.1 mV dec^{-1}). The LSV curves at different rotating speeds and the corresponding Koutecky-Levich plots are displayed in Fig. S19, and the corresponding electron transfer number (n), J_k and ECSA of 1D N-S-CMR, 2D N-S-CNS and 3D N-S-CFW are shown in Fig. 5d. Likewise, the 2D N-S-CNS possess the highest ECSA, n and J_k, indicating the most efficient ORR electrocatalyst. Meanwhile, the calculated electron transfer number is 3.95, demonstrating a four-electron transfer pathway. Fig. 5e shows the H_2O_2 yield on 2D N-S-CNS is below 10%, further confirming the four-electron transfer pathway on 2D N-S-CNS in the neutral situation. Fig. 5f shows the LSV curves of 2D N-S-CNS before and after 5000 cycles in the neutral solution, and the attenuation of $E_{1/2}$ is 4 mV after 5000 consecutive cycles, demonstrating the excellent durability of 2D N-S-CNS in a 3.5% NaCl solution.

The superior ORR performance of the 2D N-S-CNS is explained as

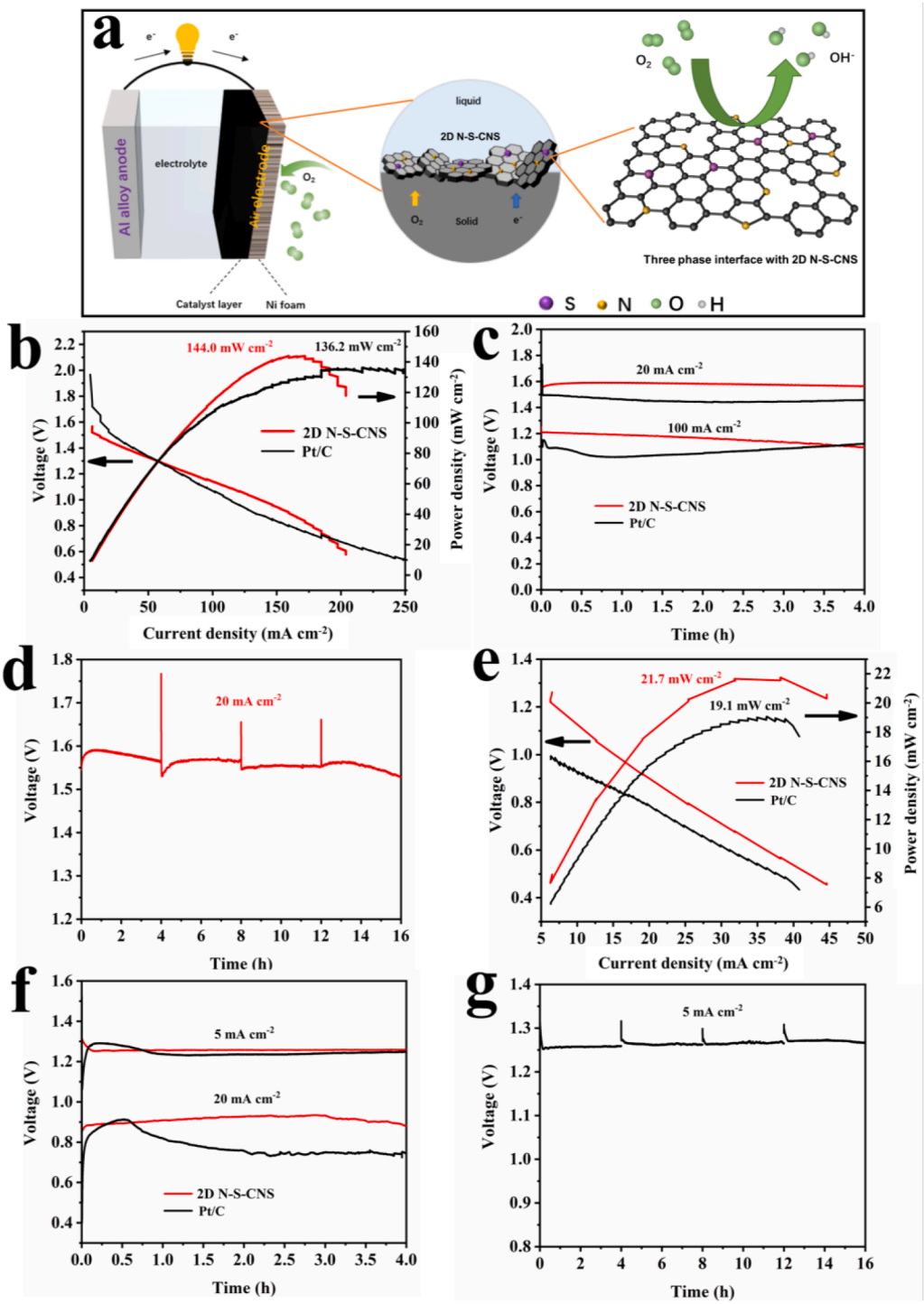

Fig. 6. (a) Illustration of the Al-air battery with the three-phase interface in the cathode. (b) current–voltage and power density curves, (c) galvanostatic discharge curves and (d) mechanical charging of the Al-air batteries with 2D N-S-CNS and Pt/C in the alkaline electrolyte. (e) current–voltage and power density curves, (f) galvanostatic discharge curves and g) mechanical charging of the Al-air batteries with 2D N-S-CNS and Pt/C in the neutral electrolyte.

follow: (1) the 2D nanosheet structure can enhance the ion and electron transfer kinetics; (2) the highest doping amount of N and S, especially the highest content of pyridinic-N species can significantly increase the activity for ORR; (3) the largest electrochemical surface area enables the most accessible active sites for ORR.

To explore the practical application, aqueous Al-air batteries based on 2D N-S-CNS air cathodes were fabricated and evaluated. Fig. 6a illustrates the structure of an Al-air battery together with the three-phase interface of the air cathode. As oxygen reduction occurs at the three-phase interface, the 2D N-S-CNS electrocatalyst with nanosheet structure can t provide massive three-phase interfaces, which can benefit the electron, ion and gas transfer for ORR [45]. Moreover, the active sites on 2D N-S-CNS can tune the absorption energy of different ORR intermediates (O_2*, OOH*, O*, OH*) [46], further reducing the external potential required for keeping all intermediate reactions exothermic [47,48]. Fig. 6b shows the current–voltage and power density curves of the Al-air batteries with 2D N-S-CNS and Pt/C electrocatalysts. The Al-air battery with 2D N-S-CNS outputs a larger working voltage than that with Pt/C at the maximum power density, and the maximum power density of the Al-air battery with 2D N-S-CNS is 144.0 mW cm^{-2}, which is slightly larger than that with Pt/C (136.2 mW cm^{-2}). In Fig. 6c, the Al-air battery with 2D N-S-CNS exhibits stable voltage plateaus of 1.59 V at 20 mA cm^{-2} and 1.18 V at 100 mA cm^{-2}, which are higher than these with Pt/C (1.50 V at 20 mA cm^{-2} and 1.15 V at 100 mA cm^{-2}). The battery can be mechanically charged by refilling an Al-Mg-Sn alloy anode after discharge, and the voltage plateau still stabilizes at 1.55 V after continuously mechanical charging (Fig. 6d), indicating the excellent durability of 2D N-S-CNS electrocatalyst. Similarly, the identical tests were also conducted in the neutral electrolyte. Fig. 6e shows the current–voltage and power density curves of the Al-air batteries with 2D N-S-CNS and Pt/C in the neutral electrolyte, and the maximum power density of the Al-air battery with 2D N-S-CNS is 21.7 mW cm^{-2}, which is also larger than that with Pt/C air cathode (19.1 mW cm^{-2}). As shown in Fig. 6f, the Al-air battery with 2D N-S-CNS also outputs stable working voltage plateaus of 1.25 V at 5 mA cm^{-2} and 0.90 V at 20 mA cm^{-2}, which are also higher than those with Pt/C air cathode (1.22 V at 5 mA cm^{-2} and 0.74 V at 20 mA cm^{-2}). The Al-air battery with 2D N-S-CNS also presents good durability in the neutral solution, and there is no voltage loss after consecutively mechanical charging.

4. Conclusions

In summary, the 1D N-S-CMR, 2D N-S-CNS and 3D N-S-CFW are prepared from carbon dots through a template-assisted strategy. When citric acid instead of carbon dots are used as precursors, the identical carbon materials with different dimensions cannot be obtained. The 2D N-S-CNS with nanosheet structure and the highest doping content of nitrogen and sulfur demonstrate the best ORR performance with half-wave potentials of 0.855 V in a 0.1 M KOH electrolyte and 0.604 V in a 3.5 wt% NaCl sodium chloride solution, which are comparable to those of Pt/C. Furthermore, the fabricated Al-air battery displays a power density of 144.0 mW cm^{-2} in the alkaline solution and 21.7 mW cm^{-2} in the neutral solution. This work provides a new approach for developing low-cost and high-performance ORR electrocatalysts for metal-air batteries.

Declaration of Competing Interest

The authors declare that they have no known competing financial interests or personal relationships that could have appeared to influence the work reported in this paper.

Acknowledgments

This work was supported by the National Natural Science Foundation of China (51874197, 51704106).

Appendix A. Supplementary data

Supplementary data to this article can be found online at https://doi.org/10.1016/j.cej.2021.130603.

References

[1] Y. Liu, Q. Sun, W. Li, K.R. Adair, J. Li, X. Sun, A comprehensive review on recent progress in aluminum–air batteries, Green Energy & Environ. 2 (3) (2017) 246–277.
[2] H. Jiang, J. Gu, X. Zheng, M. Liu, X. Qiu, L. Wang, W. Li, Z. Chen, X. Ji, J. Li, Defect-rich and ultrathin N doped carbon nanosheets as advanced trifunctional metal-free electrocatalysts for the ORR, OER and HER, Energy Environ. Sci. 12 (1) (2019) 322–333.
[3] B. Lim, M. Jiang, P.H.C. Camargo, E.C. Cho, J. Tao, X. Lu, Y. Zhu, Y. Xia, Pd-Pt bimetallic nanodendrites with high activity for oxygen reduction, Science 324 (2009) 1302.
[4] M. Shao, Q. Chang, J.-P. Dodelet, R. Chenitz, Recent advances in electrocatalysts for oxygen reduction reaction, Chem. Rev. 116 (6) (2016) 3594–3657.
[5] M. Qiao, Y. Wang, Q. Wang, G. Hu, X. Mamat, S. Zhang, S. Wang, Hierarchically ordered porous carbon with atomically dispersed FeN_4 for ultraefficient oxygen reduction reaction in proton-exchange membrane fuel cells, Angew. Chem. Int. Ed. 59 (7) (2020) 2688–2694.
[6] G. Chen, P. Liu, Z. Liao, F. Sun, Y. He, H. Zhong, T. Zhang, E. Zschech, M. Chen, G. Wu, J. Zhang, X. Feng, Zinc-mediated template synthesis of Fe-N-C electrocatalysts with densely accessible Fe-N_x active sites for efficient oxygen reduction, Adv. Mater. 32 (8) (2020) 1907399, https://doi.org/10.1002/adma.v32.810.1002/adma.201907399.
[7] S.i. Chen, L. Zhao, J. Ma, Y. Wang, L. Dai, J. Zhang, Edge-doping modulation of N, P-codoped porous carbon spheres for high-performance rechargeable Zn-air batteries, Nano Energy 60 (2019) 536–544.
[8] X. Gong, S. Liu, C. Ouyang, P. Strasser, R. Yang, Nitrogen- and phosphorus-doped biocarbon with enhanced electrocatalytic activity for oxygen reduction, ACS Catal. 5 (2) (2015) 920–927.
[9] J. Yang, F. Xiang, H. Guo, L. Wang, X. Niu, Honeycomb-like porous carbon with N and S dual-doping as metal-free catalyst for the oxygen reduction reaction, Carbon 156 (2020) 514–522.
[10] R. Paul, F. Du, L. Dai, Y. Ding, Z.L. Wang, F. Wei, A. Roy, 3D heteroatom-doped carbon nanomaterials as multifunctional metal-Free catalysts for integrated energy devices, Adv. Mater. 31 (2019) 1805598.
[11] H. Fei, R. Ye, G. Ye, Y. Gong, Z. Peng, X. Fan, E.L.G. Samuel, P.M. Ajayan, J. M. Tour, Boron- and nitrogen-doped graphene quantum dots/graphene hybrid nanoplatelets as efficient electrocatalysts for oxygen reduction, ACS Nano 8 (2014) 10837.
[12] Y. Zheng, H. Song, S. Chen, X. Yu, J. Zhu, J. Xu, K.A.I. Zhang, C. Zhang, T. Liu, Metal-free multi-heteroatom-doped carbon bifunctional electrocatalysts derived from a covalent triazine polymer, Small 16 (2020) 2004342.
[13] J. Zhu, W. Li, S. Li, J. Zhang, H. Zhou, C. Zhang, J. Zhang, S. Mu, Defective N/S-codoped 3D cheese-like porous carbon nanomaterial toward efficient oxygen reduction and Zn–Air batteries, Small 14 (2018) 1800563.
[14] K. Gao, B. Wang, L. Tao, B.V. Cunning, Z. Zhang, S. Wang, R.S. Ruoff, L. Qu, Efficient metal-free electrocatalysts from N-doped carbon nanomaterials: mono-doping and co-doping, Adv. Mater. 31 (2019) 1805121.
[15] Y. Wang, L. Tao, Z. Xiao, R. Chen, Z. Jiang, S. Wang, 3D carbon electrocatalysts in situ constructed by defect-rich nanosheets and polyhedrons from NaCl-sealed zeolitic imidazolate frameworks, Adv. Funct. Mater. 28 (2018) 1705356.
[16] X. Peng, L. Zhang, Z. Chen, L. Zhong, D. Zhao, X. Chi, X. Zhao, L. Li, X. Lu, K. Leng, C. Liu, W. Liu, W. Tang, K.P. Loh, Hierarchically porous carbon plates derived from wood as bifunctional ORR/OER electrodes, Adv. Mater. 31 (2019) 1900341.
[17] J. Zhang, Z. Zhao, Z. Xia, L. Dai, A metal-free bifunctional electrocatalyst for oxygen reduction and oxygen evolution reactions, Nat. Nanotechnol. 10 (2015) 444.
[18] X. Duan, K. O'Donnell, H. Sun, Y. Wang, S. Wang, Sulfur and nitrogen co-doped graphene for metal-free catalytic oxidation reactions, Small 11 (2015) 3036.
[19] H. Lu, C. Yang, J. Chen, J. Li, H. Jin, J. Wang, S. Wang, Tailoring hierarchically porous nitrogen-, sulfur-codoped carbon for high-performance supercapacitors and oxygen reduction, Small 16 (2020) 1906584.
[20] R. Cheng, J. Yang, M. Jiang, A. Dong, M. Guo, J. Zhang, B. Sun, C. Fu, Hierarchical porous manganese- and nitrogen-codoped carbon nanosheets derived from surface modified biomass as efficient oxygen reduction catalysts for Al-air batteries, J. Electrochem. Soc. 167 (2020), 110552.
[21] X. Zheng, J. Wu, X. Cao, J. Abbott, C. Jin, H. Wang, P. Strasser, R. Yang, X. Chen, G. Wu, N-, P-, and S-doped graphene-like carbon catalysts derived from onium salts with enhanced oxygen chemisorption for Zn-air battery cathodes, Appl. Catal. B-Environ. 241 (2019) 442–451.
[22] J. He, Y. Chen, A. Manthiram, Metal sulfide-decorated carbon sponge as a highly efficient electrocatalyst and absorbant for polysulfide in high-loading Li_2S batteries, Adv. Energy Mater. 9 (2019) 1900584.
[23] L. Bao, C. Liu, Z.L. Zhang, D.-W. Pang, Photoluminescence-tunable carbon nanodots: surface-state energy-gap tuning, Adv. Mater. 27 (2015) 1663–1667.
[24] Y. Chen, M. Zheng, Y. Xiao, H. Dong, H. Zhang, J. Zhuang, H. Hu, B. Lei, Y. Liu, A self-quenching-resistant carbon-dot powder with tunable solid-state fluorescence and construction of dual-fluorescence morphologies for white light-emission, Adv. Mater. 28 (2) (2016) 312–318.

[25] C. Chen, Z. Sun, Y. Li, L. Yi, H. Hu, Self-assembly of N doped 3D porous carbon frameworks from carbon quantum dots and its application for oxygen reduction reaction, J. Mater. Sci.-Mater. Electron. 28 (2017) 12660–12669.
[26] R. Liu, H. Zhang, S. Liu, X. Zhang, T. Wu, X. Ge, Y. Zang, H. Zhao, G. Wang, Shrimp-shell derived carbon nanodots as carbon and nitrogen sources to fabricate three-dimensional N-doped porous carbon electrocatalysts for the oxygen reduction reaction, Phys. Chem. Chem. Phys. 18 (5) (2016) 4095–4101.
[27] C. Hu, M. Li, J. Qiu, Y.-P. Sun, Design and fabrication of carbon dots for energy conversion and storage, Chem. Soc. Rev. 48 (8) (2019) 2315–2337.
[28] F. Yuan, Z. Wang, X. Li, Y. Li, Z.a. Tan, L. Fan, S. Yang, Bright multicolor bandgap fluorescent carbon quantum dots for electroluminescent light-emitting diodes, Adv. Mater. 29 (2017) 1604436.
[29] S. Li, S. Zhou, Y. Li, X. Li, J. Zhu, L. Fan, S. Yang, Exceptionally high payload of the IR780 iodide on folic acid-functionalized graphene quantum dots for targeted photothermal therapy, ACS Appl. Mater. Interfaces 9 (27) (2017) 22332–22341.
[30] R. Atchudan, T.N.J.I. Edison, Y.R. Lee, Nitrogen-doped carbon dots originating from unripe peach for fluorescent bioimaging and electrocatalytic oxygen reduction reaction, J. Colloid Interface Sci. 482 (2016) 8–18.
[31] G.A. Alsultan, N. Asikin-Mijan, H.V. Lee, A.S. Albazzaz, Y.H. Taufiq-Yap, Deoxygenation of waste cooking to renewable diesel over walnut shell-derived nanorode activated carbon supported CaO-La_2O_3 catalyst, Energy Conv. Manag. 151 (2017) 311–323.
[32] Y. Zhou, E.M. Zahran, B.A. Quiroga, J. Perez, K.J. Mintz, Z. Peng, P.Y. Liyanage, R. R. Pandey, C.C. Chusuei, R.M. Leblanc, Size-dependent photocatalytic activity of carbon dots with surface-state determined photoluminescence, Appl. Catal. B-Environ. 248 (2019) 157–166.
[33] F. Niu, J. Yang, N. Wang, D. Zhang, W. Fan, J. Yang, Y. Qian, $MoSe_2$-covered N, P-doped carbon nanosheets as a long-life and high-rate anode material for sodium-ion batteries, Adv. Funct. Mater. 27 (2017) 1700522.
[34] S. Yang, L. Zhi, K. Tang, X. Feng, J. Maier, K. Müllen, Efficient synthesis of heteroatom (N or S)-doped graphene based on ultrathin graphene oxide-porous silica sheets for oxygen reduction reactions, Adv. Funct. Mater. 22 (17) (2012) 3634–3640.
[35] H.B. Yang, J. Miao, S.-F. Hung, J. Chen, H.B. Tao, X. Wang, L. Zhang, R. Chen, J. Gao, H.M. Chen, L. Dai, B. Liu, Identification of catalytic sites for oxygen reduction and oxygen evolution in N-doped graphene materials: development of highly efficient metal-free bifunctional electrocatalyst, Sci. Adv. 2 (2016), e1501122.
[36] C. Hu, L. Dai, Multifunctional carbon-based metal-free electrocatalysts for simultaneous oxygen reduction, oxygen evolution, and hydrogen evolution, Adv. Mater. 29 (2017) 1604942.
[37] S.L. Zhang, B.Y. Guan, X.W. Lou, Co–Fe alloy/N-doped carbon hollow spheres derived from dual metal–organic frameworks for enhanced electrocatalytic oxygen reduction, Small 15 (2019) 1805324.
[38] J.-Y. Zhao, R. Wang, S. Wang, Y.-R. Lv, H. Xu, S.-Q. Zang, Metal–organic framework-derived Co_9S_8 embedded in N, O and S-tridoped carbon nanomaterials as an efficient oxygen bifunctional electrocatalyst, J. Mater. Chem. A 7 (13) (2019) 7389–7395.
[39] L. Lai, J.R. Potts, D. Zhan, L. Wang, C.K. Poh, C. Tang, H. Gong, Z. Shen, J. Lin, R. S. Ruoff, Exploration of the active center structure of nitrogen-doped graphene-based catalysts for oxygen reduction reaction, Energy Environ. Sci. 5 (7) (2012) 7936, https://doi.org/10.1039/c2ee21802j.
[40] Y. Su, Y. Zhang, X. Zhuang, S. Li, D. Wu, F. Zhang, X. Feng, Low-temperature synthesis of nitrogen/sulfur co-doped three-dimensional graphene frameworks as efficient metal-free electrocatalyst for oxygen reduction reaction, Carbon 62 (2013) 296–301.
[41] B. Liu, M. Yang, H. Chen, Y. Liu, D. Yang, H. Li, Graphene-like porous carbon nanosheets derived from salvia splendens for high-rate performance supercapacitors, J. Power Sources 397 (2018) 1–10.
[42] Z. Sun, Y. Wang, L. Zhang, H. Wu, Y. Jin, Y. Li, Y. Shi, T. Zhu, H. Mao, J. Liu, C. Xiao, S. Ding, Simultaneously realizing rapid electron transfer and mass transport in jellyfish-like Mott-Schottky nanoreactors for oxygen reduction reaction, Adv. Funct. Mater. 30 (2020) 1910482.
[43] X. Wang, Y. Jia, X. Mao, D. Liu, W. He, J. Li, J. Liu, X. Yan, J. Chen, L. Song, A. Du, X. Yao, Edge-rich Fe−N_4 active sites in defective carbon for oxygen reduction catalysis, Adv. Mater. 32 (2020) 2000966.
[44] H.W. Kim, V.J. Bukas, H. Park, S. Park, K.M. Diederichsen, J. Lim, Y.H. Cho, J. Kim, W. Kim, T.H. Han, J. Voss, A.C. Luntz, B.D. McCloskey, Mechanisms of two-electron and four-electron electrochemical oxygen reduction reactions at nitrogen-doped reduced graphene oxide, ACS Catal. 10 (1) (2020) 852–863.
[45] T. Zhang, H. Zhou, From Li–O_2 to Li–Air batteries: carbon nanotubes/ionic liquid gels with a tricontinuous passage of electrons, ions, and oxygen, Angew. Chem. Int. Ed. 51 (2012) 11062–11067.
[46] H.Y. Su, Y. Gorlin, I.C. Man, F. Calle-Vallejo, J.K. Nørskov, T.F. Jaramillo, J. Rossmeisl, Identifying active surface phases for metal oxide electrocatalysts: a study of manganese oxide bi-functional catalysts for oxygen reduction and water oxidation catalysis, Phys. Chem. Chem. Phys. 14 (2012) 14010–14022.
[47] M. Jiang, C. Fu, R. Cheng, T. Liu, M. Guo, P. Meng, J. Zhang, B. Sun, Interface engineering of Co_3Fe_7-Fe_3C heterostructure as an efficient oxygen reduction reaction electrocatalyst for aluminum-air batteries, Chem. Eng. J. 404 (2021), 127124.
[48] M. Jiang, C. Fu, R. Cheng, W. Zhang, T. Liu, R. Wang, J. Zhang, B. Sun, Integrated and binder-free air cathodes of Co_3Fe_7 nanoalloy and $Co_{5.47}N$ encapsulated in nitrogen-doped carbon foam with superior oxygen reduction activity in flexible aluminum-air batteries, Adv. Sci. 7 (2020) 2000747.